# Automating building element detection for deconstruction planning and material reuse: A case study

**Author(s):**
Gordon, Matthew ⬡; Batallé, Anna; De Wolf, Catherine; Sollazzo, Aldo; Dubor, Alexandre; Wang, Tong
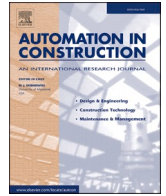
# Automating building element detection for deconstruction planning and material reuse: A case study

Matthew Gordon [a,b,*], Anna Batallé [c], Catherine De Wolf [a], Aldo Sollazzo [b], Alexandre Dubor [b], Tong Wang [c]

[a] *Institute of Construction and Infrastructure Management, ETH Zurich, Stefano-Franscini-Platz 5, 8093 Zurich, Switzerland*
[b] *Institute for Advanced Architecture of Catalonia, Carrer de Pujades 102, 08005 Barcelona, Spain*
[c] *Department of Management in the Built Environment, TU Delft, Julianalaan 134, Building 8, 2628 BL Delft, Netherlands*

## ARTICLE INFO

## ABSTRACT

To address the need for a shift from a linear to a circular economy in the built environment, this paper develops a semi-automated assistive process for planning building material deconstruction for reuse using sensing and scanning, Scan-to-BIM, and computer vision techniques. These methods are applied and tested in a real-world case study in Geneva, Switzerland, with a focus on reconstruction and recovery analysis for floor beam systems. First, accessible sensing and scanning tools, such as mobile photography and smartphone-based consumer-grade Lidar devices, are used to capture imagery and other data from an active demolition site. Then, photogrammetry and point cloud data analysis are performed to construct a 3D BIM model of relevant areas. The structural relationships between reconstructed BIM elements are evaluated to score the feasibility for recovery of each element. This study illustrates what is feasible and where further development is necessary for automating building material reuse planning at scale to increase the uptake of circular economy practices in the construction sector.

## 1. Introduction

The construction industry represents 5.6% of the European Gross Domestic Product [1], yet it is the largest consumer of global raw materials [2], responsible for 39% of anthropogenic greenhouse gases [3] and 35.9% of the total solid waste generated [4]. Through the Waste Framework Directive, the EU aimed at recovering 70% of construction and demolition waste by 2020, thereby reducing the amount of debris going to landfill [5]. During the most recent progress study for the Framework Directive, more than half of member states were on track for this goal as of 2018 [6], however a broader study of environmental policy as of 2022 indicated more than half had not ultimately reached these goals [7]. Specifically, contemporary recovery directives treat reuse, recycling, and backfilling operations as material recovery [5], the latter of which still creates an end of life for the product. This is part of a broader trend wherein current waste efforts have largely resulted in downcycling practices whereby a material's original developed properties are lost and the new use is of lesser value [8]. Additionally, given the accompanying rise in consumption, reused and recycled materials

only account for 11.8% of overall material usage [9].

To address the resource depletion, waste generation, and pollution caused by the construction sector, an urgent shift from a linear 'take–use–waste' model to a circular economy is needed, in which building components have multiple or extended lifespans [10]. The scale of the issue is illustrated in a study on the residential building material stocks in Switzerland, which estimated 2.6 million tons of material outflow per year as of 2015, and predicted to reach 6.1 million tons per year by 2055 [11]. Extending the lifespan of the current material stock through reuse is an extensive process, as buildings pose complex, multi-variant problems that are addressed by numerous stakeholders often lacking collaboration, while changing practices and synergies within the industry produce organizational challenges [12]. Given this, the exploration and adoption of digital technologies could enable a shift toward the circular paradigm in the Architecture, Engineering and Construction (AEC) sector [13], with the goal of carbon-free buildings by 2050, in line with the Glasgow Climate Pact [14,15]. In particular, digitizing and automating the process of material reuse in the built environment can facilitate the connection of actors across the value chain through a

common methodology by enabling information gathering and sharing [16].

The 9R Strategies Framework [17] encapsulates the primary strategies by which lifespans of building components can be improved. Critical among them for the building sector are the *reuse* of components once removed, *repair* of components in place when possible, *refurbishment* of removed components for new use, *remanufacture* of discarded parts of a component, and *recycling* of any waste still produced, preferably using techniques that avoid downcycling [18]. The complexity and breadth of information required for effective material application of these strategies has led to several specializations among groups in the industry. At the comprehensive information scale, groups such as Building Material Scout in Germany [19] and Zirkular in Switzerland [20] offer design consulting and matchmaking with other circular service providers, while Opalis in Belgium [21] provides information on local material dealers as well as product and technical information from a recovery standpoint. This indicates a need for an expansion of the traditional array of BIM data provided with building products. One implementation includes the material passport system developed by groups such as Buildings as Material Banks [22].

At the level of specific components, groups such as useagain in Switzerland [23] and Enviromate in the UK [24] provide marketplaces and inventory and tracking systems for components and disassembled materials on a per-site basis, while Excess Material Exchange in the Netherlands [25] brings these matching services to a range of possible corporate waste materials. The materials may be already recovered and in storage, or in buildings scheduled for impending deconstruction. While listings contain a variety of per-element data, at minimum they cover element counts and approximate dimensions, to be matched with new designs.

The on-site recovery of materials is performed by deconstruction groups. Companies with deconstruction arms include New Horizon in the Netherlands [26], RotorDC in Belgium [27], and Materiuum in Switzerland [28]. Within a particular site, components may be chosen for recovery based on current market needs, accessibility, and removal potential or quality. Currently, deconstruction groups rely on manual inspection by experts to produce inventories of recoverable components and materials, limiting the maximum throughput and turnaround time of materials.

Common to these roles is the applicability of BIM-integrated material information, for which automation and digitization technologies can be applied to produce at scale. The reuse benefits of this digital tooling are also complemented by the economic benefit for the relevant users, as building sector digitization has been predicted to lead to 13–21% cost savings during the engineering and construction phases, and 10–17% savings during operations [29].

The research undertaken in this project aims at building more knowledge on digitalized strategies for a circular building environment, in line with the EU's strong ambition for the new European Bauhaus [30] to help Europe move toward circularity and digitalization. Based on data capture performed on a real demolition site undergoing recovery, this research develops a site-digitization and inventory-making procedure focused on steel beam-and-column systems, for use when planning deconstruction jobs (outlined in Fig. 1). This procedure covers the combined problem domains of handling data from low-cost capture sources (necessary at large scales of capture) and the specific challenges of structural steel geometry and relationships. First, we describe the state of the art in digitization and Scan-to-BIM technology (*Section 2*). A relevant recovery area of the test site is digitized using several capture hardware methods (*Section 3.1–3.3*) Our data processing starts with cleaning and normalizing the digitized site information (*Section 3.4*) and identifying critical areas (*Section 3.5*). Then, two alternatives for locating beams within each area are tested, based on established Scan-to-BIM methodologies (*Section 3.6*). Next, relevant columns for each system are located (*Section 3.7*). Finally, the connection logic across the beam system is determined to measure the complexity of each component's recoverability based on its relative accessibility (*Section 3.8*). Taken together, the output of this technology is envisioned as a direct source for contemporary material marketplaces and design tools.

## 2. Background

### 2.1. Reality capture to digitized demolition sites

Reality capture has been extensively studied in AEC as a method of digitizing historic sites, verifying as-built details, and tracking new work against a known digital model [31–34]. Verification is often specifically applied in the mechanical, electrical and plumbing (MEP) domain, given the large amounts and difficult accessibility of relevant components [35,36]. Photogrammetry (taking real-world measurements from 2D imagery) provides the common contemporary method of structure from motion (SfM), which estimates three-dimensional points using the overlap and parallax between a series of still images. Alternatively, Lidar scanning performs direct measurements by measuring the time of flight (TOF) of a reflection of a laser in the scene. While typically performed from a tripod, handheld full-size and smartphone-based models exist. These can generally attain 1 cm accuracy, however their smaller range may present issues for AEC applications, with the Apple Lidar having a maximum range of 5 m [37,38].

Building scale photogrammetry has generally been based on handheld or unmanned aerial vehicle (UAV, i.e. drone), −mounted perspective cameras, though it has been found that spherical or 360-degree photography can achieve point-location accuracy similar to that of Lidar systems above a minimum distance [39]. Comparisons of photogrammetry from smartphone imagery compared to full-sized cameras has indicated a twofold increase in discrepancy for in-image and geometric measurements, though it is noted the differences are rapidly shifting. [40].

Lidar and other TOF systems measure real distance information, so the scale of their output inherently matches reality. On the other hand,
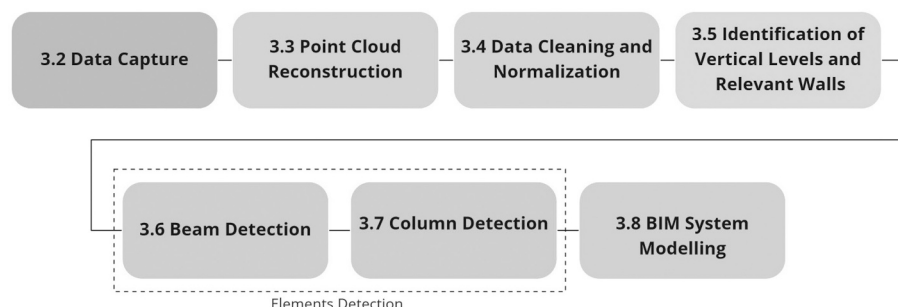


**Fig. 1.** Overview of analysis steps, numbered by section.

SfM photogrammetry at its core works only with scale-less image data, so external information is included for accurate scaling to reality. Commonly this is performed semi-automatically with the inclusion of tags at pre-measured positions or objects of known size in the scene. However, this involves additional operator effort, especially for very large or minimally connected interior spaces. Inherent position information can be utilized if the camera includes global navigation satellite system (GNSS) information (such as a smartphone), as is often used at the UAV-topography scale [41]. However, satellite signals are often unavailable in the building interior context and contemporary smartphone GNSS resolution produces scaling errors of 10% at best [42].

Additionally, photogrammetry may produce clouds at arbitrary orientations. Editing is required to align at least the floor of the scene with the XY plane, and often the major walls with the X- and Y- axes. A case in which a scene is entirely describable along these axes is described as a Manhattan World (MW) scenario, one of several models for describing the complexity and reducibility of a 3D scene [43,44]. A possible strategy for automatic alignment (pose normalization) on indoor datasets finds trends in the normals of the cloud's points and optimizes their alignment to the world axes [45].

Compared to exterior reality-capture operations, indoor scanning must deal with greater amounts of clutter and extraneous objects that may occlude relevant geometry or become confused with permanent structures. While in some domains this can be solved by an initial semantic segmentation (labeling and splitting of datapoints by known present classes, e.g. furniture) [46,47], in the construction sector many clutter items may not consistently appear in a known class. A generalized method that handles clutter outside the primary area checks the visibility of relevant areas by ray casting, ignoring outliers and clutter points [48]. Another solution employs heuristics on the point cloud's normals, which excludes all normals more than a specific distance from the expected vertical or horizontal planes, relevant to common BIM element types [49]. Per-point analysis may be expanded by additional contextual features that describe the local topology [50]. Some context analysis also utilizes initial voxelization to simplify the description of local patches and make non-clutter forms more obvious [51]. In further scenarios, additional hardware may be utilized, such as the inclusion of radio-frequency identification (RFID) tags for furniture in commonly scanned spaces, allowing the lookup and matching of the associated explicit geometry [52].

For applications where raw 3D data would be overly complex, computer vision (CV) techniques have been brought to the construction site in various capacities. A common application is for structural inspection, whereby the techniques can help locate issues such as concrete cracks, steel corrosion, and steel delamination [53]. Identification of material types is another primary application, and a support-vector-machine (SVM)-based classification system has been developed specifically for building materials for use in progress monitoring. [54]. Considering individual elements, state-of-the-art segmentation models such as Mask R-CNN have been employed as a foundation for reconstructing 3D elements from minimal input images for use with BIM [39].

For all applications, the complexity and disorder of clutter and backgrounds in building sites is of concern, as these factors have been noted to strongly limit object recognition accuracy [55].

### 2.2. Dataset generation of construction components through scan-to-BIM

Methods for automatic BIM reconstruction feature a mix of supervised and unsupervised tasks. As these methods do not have existing documentation for comparison, they must accommodate a large variety of possible input scenarios. Initially, simple geometric features or predicted segments are localized, at which point methods are applied to combine and classify these areas into BIM geometry [56].

One accepted approach to identify Manhattan World-aligned elements is via point density histograms across different axes. For instance, for indoor wall reconstruction, predictions for wall locations can be found along maxima in histograms of point density [57]. Further developments of this technique use these locations to split a total building volume, which is then progressively re-combined according to rules of room connection to create the final form [58]. These statistical methods may lead to limits in the variety of spaces able to be analyzed, which can be avoided by considering the site as a series of volumetric convex cells in which wall, floor, and void geometry are calculated for equally [48].

Alternatively, analysis can be performed from a 2D plan perspective, with a subset of the cloud flattened to two dimensions and relevant points projected to the ground plane. Hough transforms, traditionally used for edge detection in computer vision [59], can then be applied along with clustering to determine local and regional directionality and thus edges on walls [49,57]. These edges are then iteratively combined into complete wall segments.

Additionally, analytical complexity increases for BIM elements with higher geometric complexity. For example, direct analysis of the local point cloud region can be used for extracting dimension, direction, and profile for steel elements. However, the initial segmentation of the relevant points from the rest of the cloud must still be performed manually first [60].

The specific applications of Scan-to-BIM systems define the types of data that are focused on. For instance, construction verification considers absolute positions and surface level deviations, heritage digitization may largely focus on element detailing, and demolition actors will have use for accurate volumes of material, or per-element dimensions and relative positions between elements. As a midpoint between BIM verification and BIM reconstruction, some applications track the temporary works including scaffolding and formwork, by considering the space around explicitly modeled elements to work with points where temporary components are likely to exists [61].

The details of geometric analysis for Scan-to-BIM vary with the chosen BIM categories and application (Table 1). Common domains include walls and slabs to generate room layouts, the verification of as-built MEP, and verification or defect detection in structural concrete. Steel structural components present particular challenges, as they are often smaller in cross section, have more complex profiles (and thus

**Table 1**
Selection of Scan-to-BIM studies.

| Reference | Methods | Tested categories | Application |
|---|---|---|---|
| Son 2017 [63] | convexity analysis | concrete structural elements | producing new models |
| Xu et al. 2018 [64] | random forest with LSSHOT descriptor | scaffolding | producing new models |
| Ochman 2019 [48] | ILP | walls, floors, rooms | producing new models |
| Yang 2020* [60] | PCA, cross section fitting | steel structural elements | producing new models |
| Guo et al. 2021 [62] | feature-based global registration | steel structural elements | deformation monitoring |
| Kim 2021 [65] | deep learning, connectivity relations | concrete structural elements | producing new models |
| Valero et al. 2021 [36] | histogram analysis, voxel clustering, polygon matching | slabs, walls, MEP | producing new models |
| Kaufmann et al. 2022 [66] | RANSAC, H-obb | concrete slabs, walls, columns | producing new models |
| Wang 2022 [67] | deep learning | MEP | producing new models |

smaller continuous planes), and have more opportunities for self-occlusion. This makes full process automation difficult, leading to the need for manual pre-segmentation [60] or working within a specific pre-known structural system [62].

### 2.3. Building logic for deconstruction assessment

Digitally assisted analysis can support the end user in managing the density of data in BIM models. Effective analysis is dependent on the software's ability to handle both explicit information in the BIM data and implicit relationships that a human would be able to discern. This deduction has been tested with the application of unsupervised and supervised machine learning techniques to open-format BIM data [68]. The specifics of BIM element relationships are also critical when planning a building's deconstruction. Though generally encoded in textual building codes and domain knowledge, some methodologies for building analysis have defined the relations of building components as formal rules. Applications include discrete structural analysis [69] as well as multidisciplinary design optimization [70]. Rule-based analysis has also been applied on a component-specific level to the topic of component connections and construction sequencing [71]. In a broader view, these techniques can model the relationships of differing component lifespans within a building, along with its overall transformability [72].

## 3. Materials and methods for digitization of deconstruction sites

### 3.1. Test site overview

The inventory-making procedure was tested at a warehouse site being demolished in Geneva, Switzerland. While the site contained various types of recoverable components, a steel-frame mezzanine was chosen to evaluate the reconstruction process (Fig. 2).

### 3.2. Data capture

Data capture was conducted via two main methods: photogrammetry and mobile-device-based Lidar scanning, low-cost methods applicable to the large quantity of sites that will ultimately require digitization. Photogrammetry imagery was captured using still photography from a mobile device and 360-degree video capture. Lidar capture was performed using a 2021 Apple iPhone 12 Pro. The hardware was accessed with the software systems 3D Scanner App, Polycam, and Pix4D (hereafter referred to as Lidar 1, 2, and 3, respectively). These systems

exported either point clouds directly as an output, or textured meshes from which the vertices were extracted. All point clouds were captured in a single pass; the registration of clouds from multiple areas was not considered in this study.

In order to test the reconstruction methods across these different capture devices, a subset of possible per-point metadata was chosen for final analysis. Information specific to the capture method – such as capture position, point intensity, or local reconstruction confidence – was not utilized, in order to only compare the effects of their noise and accuracy. Per-point geometric information, such as local density and normals, were calculated if necessary and used during the pre-processing steps (*Section 3.4*). The main BIM reconstruction analysis methodology ultimately worked only with point position as input.

Finally, the test area was manually measured and modeled both to provide a ground truth to test BIM reconstruction accuracy, and to generate synthetic ideal point clouds to evaluate the effects of each scanning method's noise and error against a baseline (Fig. 3). Face to face measurements were made by hand for all relevant components in the area, and for the dimensions of all relevant components.

### 3.3. Software overview

Photogrammetry was performed using Agisoft Metashape v1.7.1, which has been found to produce results applicable to indoor reconstruction [73,74]. Relevant tradeoffs between photogrammetry software methods include resistance to noise, time of processing, adaptability to different image types, and effects of the software's original intended scale (e.g. terrain or furniture). Point cloud transformation and cleaning were performed with CloudCompare v2.12. Point cloud analysis operations were written using the Open3D v12 library for Python.

### 3.4. Data cleaning and normalization

After capture, each cloud was spatially sub-sampled to 10 mm for more efficient processing and to reduce local variation in point density. This resolution matches the subsampling step of other contemporary Scan-to-BIM studies [36,67].

Errors in the photogrammetry process consist of matching errors (spatial offsets of real geometry) and background noise (points at non-existent geometry) [64]. Background noise was removed by identifying points and clusters of points that had resulted from incorrect matching between frames (Fig. 4). First, a Statistical Outlier Removal filter was applied with a neighborhood of 6 points and a standard



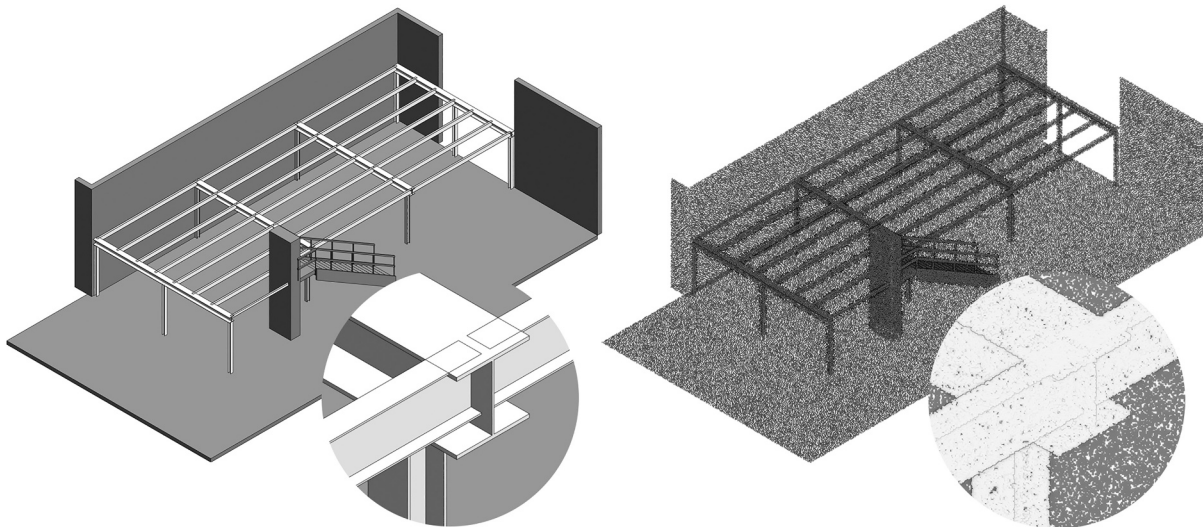**Fig. 2.** Overview of test location (left), typical connection at location (right).

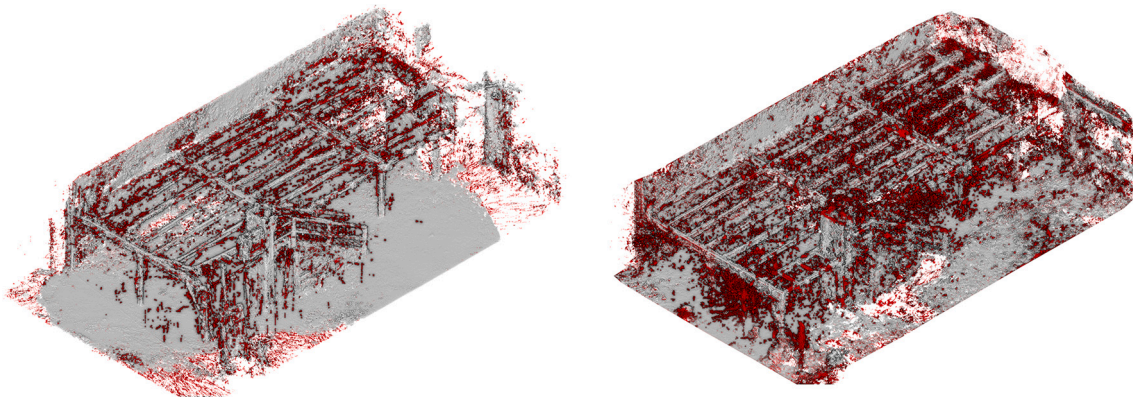**Fig. 3.** Ground truth BIM model (left) and example synthetic point cloud (subsampled to show detail).



**Fig. 4.** Example of aligned and cleaned clouds from still image photogrammetry (left) and 360 video photogrammetry (right). Removed points are indicated in red. (For interpretation of the references to colour in this figure legend, the reader is referred to the web version of this article.)
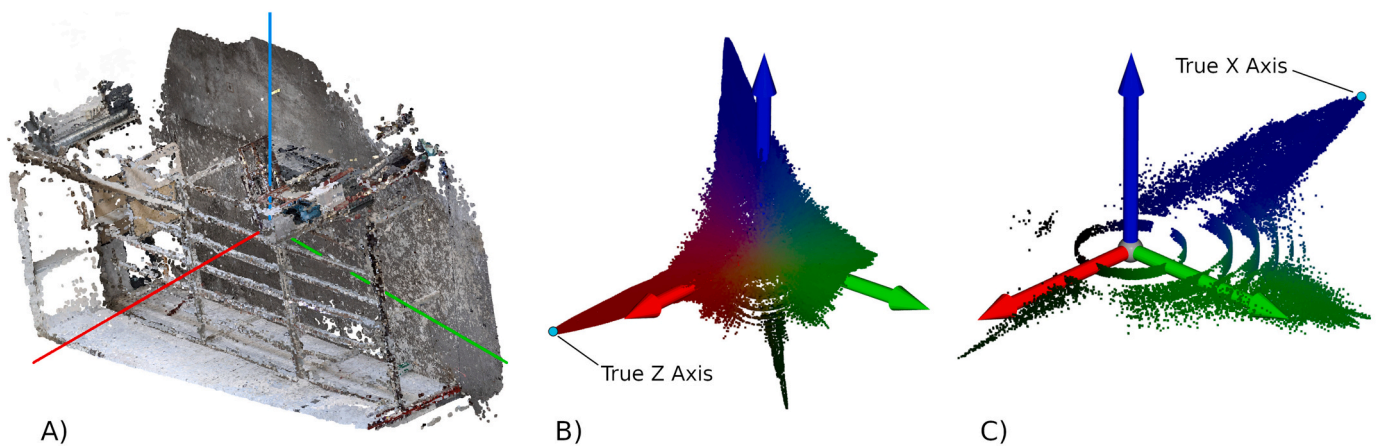


A)  B)  C)

**Fig. 5.** The photogrammetry cloud was initially generated misaligned with the world axes, which would prevent correct analysis (A). The EGI for the cloud's normals illustrates this skew (B). The densest direction (true Z-axis) is marked with a cyan point. After rotation, only the predominately horizontal vectors are shown (C), and the calculated true X-axis is again marked in cyan. For visualization, each EGI point's distance from the origin is scaled by its local density. (For interpretation of the references to colour in this figure legend, the reader is referred to the web version of this article.)

deviation factor of 1.0, removing points significantly distant from their neighbors [75]. Additionally, Radius Outlier Removal was applied at each point, taking a point count of a region of radius 0.25 m, and removing points with fewer than 2650 neighbors in their region [75]. These parameters were determined experimentally against the density of noise produced from this photogrammetry pipeline. Matching errors were not removed at this step, and their influence was thus observed in the final error results.

Each photogrammetry cloud was initially scaled using a 60 cm metal rod as a reference object, placed to be visible in the majority of capture angles. The scaling was checked using manual spot measurements of the distance between the flat faces of the columns to ensure that it could be properly compared to the ground truth. Although generally measuring true distances, the Apple Lidar system has an observed per-point mean error of 1–2 cm [37,76], and total error at the building scale of up to 10 cm [77]. As this final discrepancy is due to non-linear errors during the mobile trajectory reconstruction, there was no attempt to correct it using scaling.

Each cloud was then aligned automatically to the coordinate system's main axes (pose-normalized) to prepare it for further analysis, using a variation on Hubner's method [45] (Fig. 5). Photogrammetry results required an initial alignment of the scene's Z-axis, and all methods required additional rotation-normalization around this Z-axis, as all later analysis required data closely following the Manhattan World model. Normalization was applied by taking the extended Gaussian image (EGI), a point cloud created from a summary of the main point cloud's normal vectors, in order to identify trends in the scene's orientation. Each normal vector was weighted by the point density of its local neighborhood (within 0.3 degrees between vectors) in the sphere, and the point with the greatest value was considered to represent the vector for the scene's true Z-axis. The simplest transformation from this vector to the world Z-axis (0,0,1) was recorded and applied to the EGI.

Next, only points near the transformed EGI's XY-plane were considered to limit the analysis to normals coming from walls (Fig. 5, C). The largest density value was again found among this subset, and the vector considered to be the scene's X-axis. The rotation to this vector was applied to the total transformation, and the transformation was applied to the original point cloud (Fig. 4).

Lastly, the cloud was translationally aligned with the ground truth model for comparison, using the Iterative Closest Point method. The scale and Z-axis of the resulting transformation were locked to maintain effects of the capture and alignment methods.

The total normalization operation thus produced a cloud appropriate for use with the chosen analysis methods and comparable to the ground truth model.

### 3.5. Identification of vertical levels and relevant walls

For BIM element reconstruction, the approximate areas encompassing the beam systems were first located in the form of horizontal slices of the space. The location was determined by histogram analysis of each point cloud along the cloud's Z-axis. Based on the total bounding box of the cloud, the histogram was divided into bins such that each bin represented the point count of a 50 mm area. The histogram was then smoothed with a nearest-neighbor kernel of 3 bins in width and the totals of each bin were normalized to remove differences in average point density between capture methods (scaled such that the maximum value was 1). The peaks were calculated with a minimum prominence of 0.1, a minimum width of 3 bins (150 mm), and a relative height of 0.5 (Fig. 6); these values were determined experimentally and may be specific to factors such as camera model and photogrammetry algorithm. This method detected all strong horizontal geometries, including floors as well as the desired beam systems.

To avoid false positives and to separate Z-slices representing floors from beam systems, a simple measure of point density was taken. First, the points of each slice were projected to the 2D plane. The slice was then rendered as an image, with each point filling a single pixel, at two different scales: 40 mm/px and 200 mm/px (Fig. 7). The images were then rescaled to the same size, the number of highlighted pixels was counted, and the counts were compared between scales. In this operation, greater downscaling filled in more pixels for slices with a large 'surface area' between the geometry and open space. Z-slices where the larger scaling had <50% the coverage score of the smaller scaling were considered to be true beam layers. This complete layer-determination step is described in Algorithm 1 in the appendix.
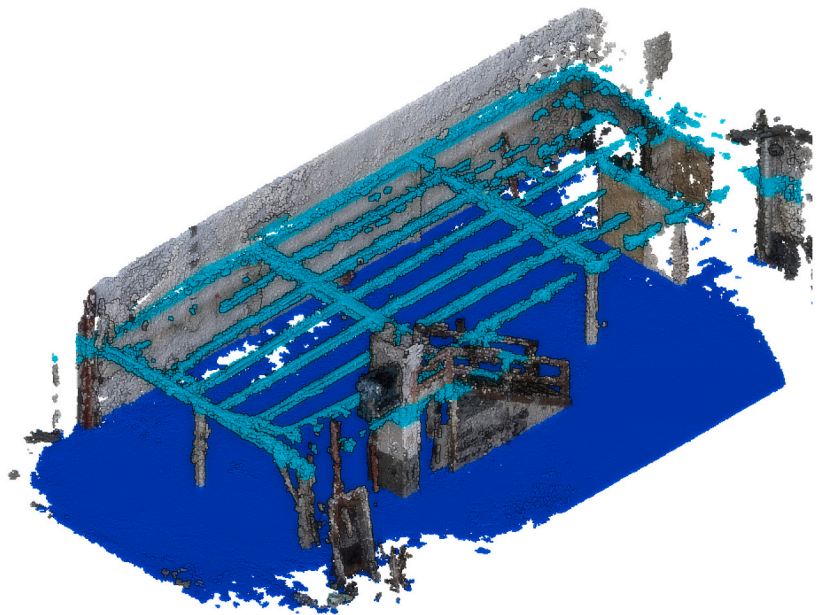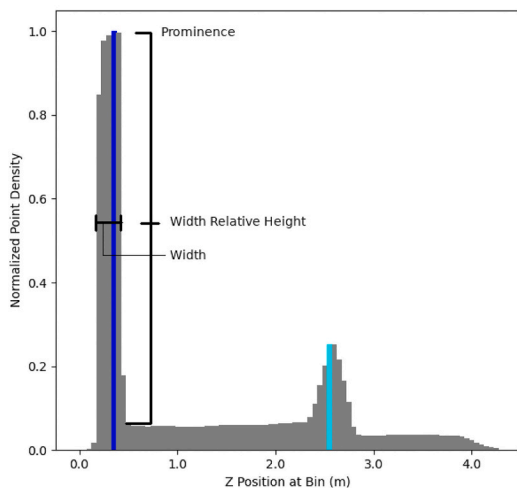


**Fig. 6.** Plot of *Z*-axis point-count histogram for the still image photogrammetry cloud; each bar represents the point count of each 50 mm horizontal slice of the cloud; values are normalized to avoid differences in point density. Detected peaks are shown in blue and cyan (indicating the floor and beam layers, respectively). (For interpretation of the references to colour in this figure legend, the reader is referred to the web version of this article.)
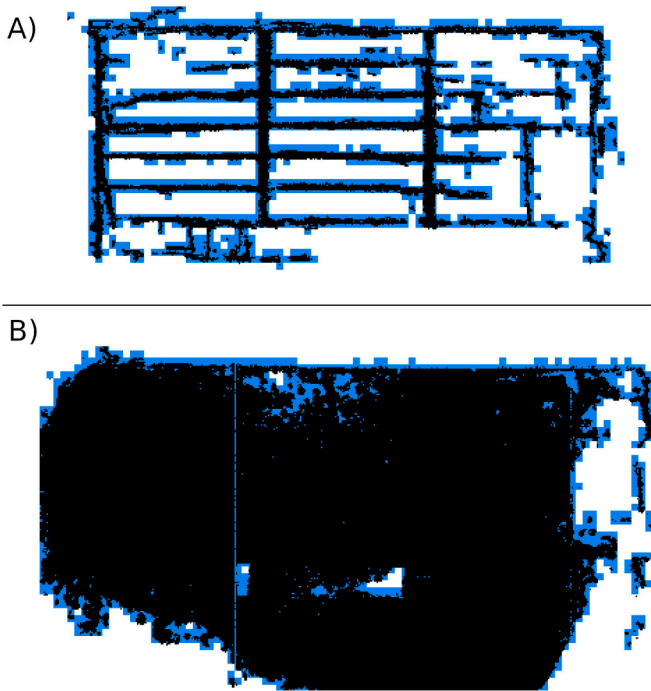
**Fig. 7.** Comparison of two Z-levels showing peaks in the photogrammetry scan of Area 1. The 40 mm/px image is indicated in white, and the additional pixels filled in at 200 mm/px indicated in blue. The true beam layer (A) has a ratio of 0.47 between scales, and the floor layer (B) has a ratio of 0.90. (For interpretation of the references to colour in this figure legend, the reader is referred to the web version of this article.)

### 3.6. Beam detection and location

Given the complexity of analyzing unstructured point cloud data in its fully 3D form, the analysis methods tested first flattened the data into a simpler form, to use existing statistical and computer vision methods to identify the likely locations of BIM elements. This was made possible by the Manhattan World nature of the test location.

#### 3.6.1. Beam detection using 1D histogram analysis

The first method evaluated took advantage of the linear nature of the elements. Within each previously determined beam system slice, point density histogram analysis was again applied along the X- and Y-axes, for determining candidate beam locations. In each histogram, peak finding was again applied, here using a prominence of 1.3 and a width of 4 (200 mm), taken at a relative height of 0.75 (Fig. 8). Here, the required prominence (a measurement of the local height) was the strongest differentiator between a peak considered relevant vs. a peak from noise.

From each of these locations, the dimensions of the beam were determined by measuring changes in value around each peak. Starting from the peak bin, the considered region was expanded in each direction until the difference from the peak passed a relative threshold.

(Fig. 9). This defined an initial bound, from which points were cropped from the original cloud to determine the final beam size based on their maximum bounds.

#### 3.6.2. Beam detection using 2D Hough transforms

The second method considered for identifying beam locations analyzed the beam region as a 2D system, utilizing computer vision techniques. The cloud was first rendered as a 2D image with colour representing density value (heatmap) at a scale of 1 px/10 mm (matching the subsampling resolution to avoid artifacts) and each point contributing to a 10 px region around its location, (matching the expected per-point worst-case accuracy errors) (Fig. 10, A). The heatmap values were normalized, with the densest pixel scaled to a value of 255. The binary threshold of this heatmap was taken with a cutoff of 22, which was determined experimentally to be the value closest to the true
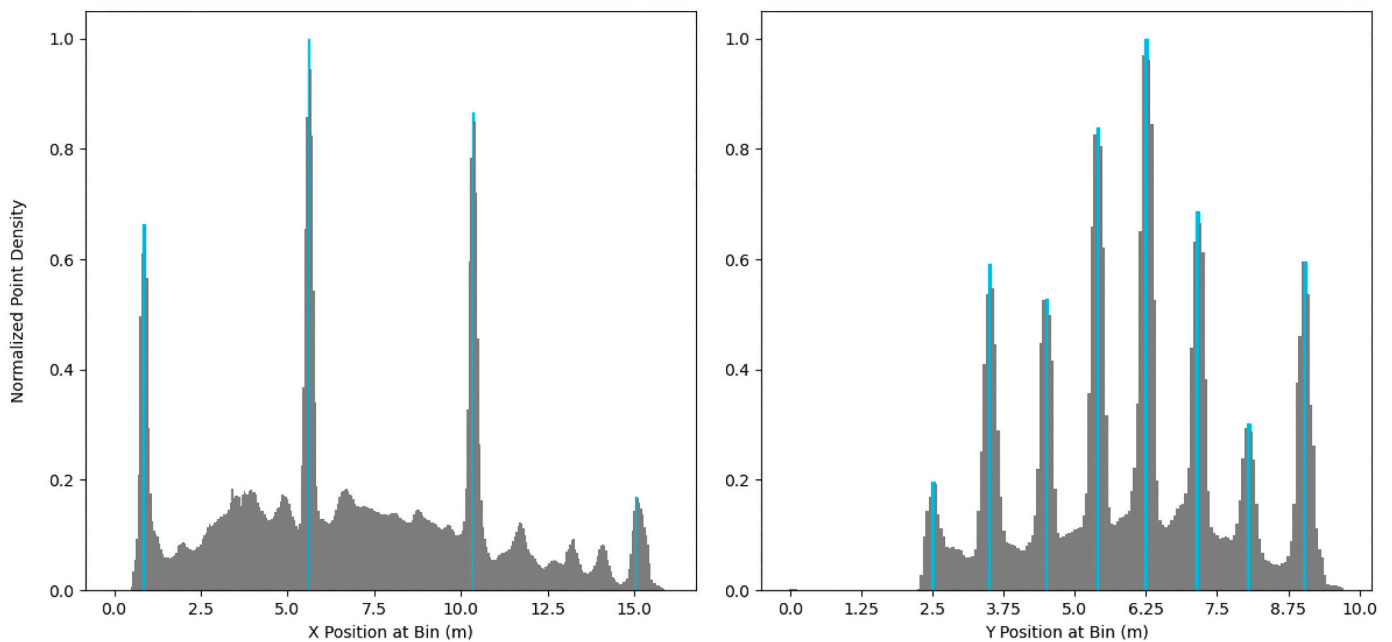


**Fig. 8.** Histogram of point concentration in Z slice along X- and Y- axes in the test area. Each bar represents the point count of a 50 mm slice of the cloud. Values are normalized to avoid differences in point density. Cyan indicates detected peaks. (For interpretation of the references to colour in this figure legend, the reader is referred to the web version of this article.)
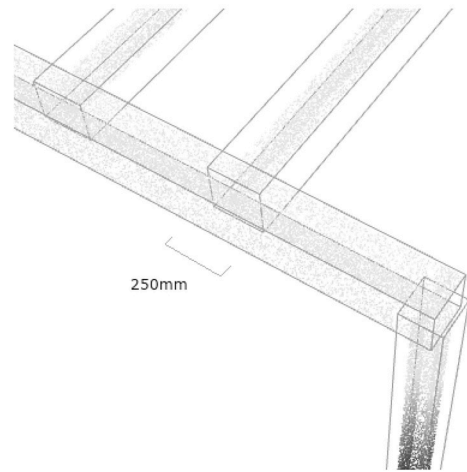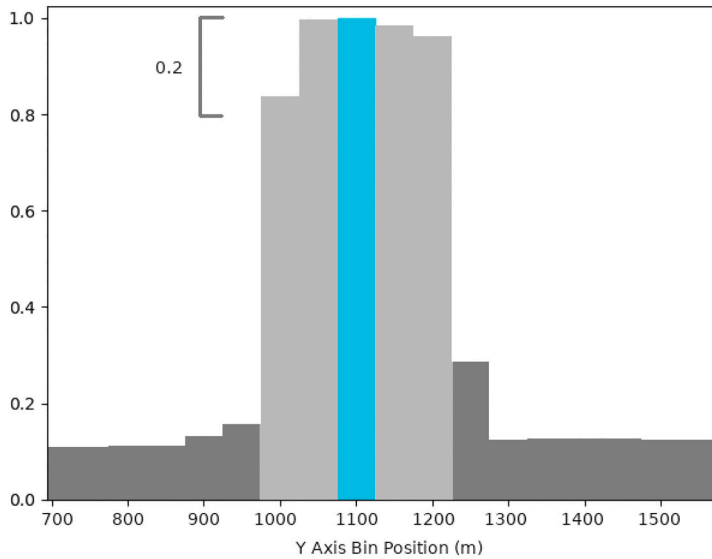
**Fig. 9.** An example peak has a neighborhood of 5 bins (250 mm) in which the histogram is within the relative threshold difference of 0.2. Thus, a 250 mm-wide region is cropped to obtain final beam points.
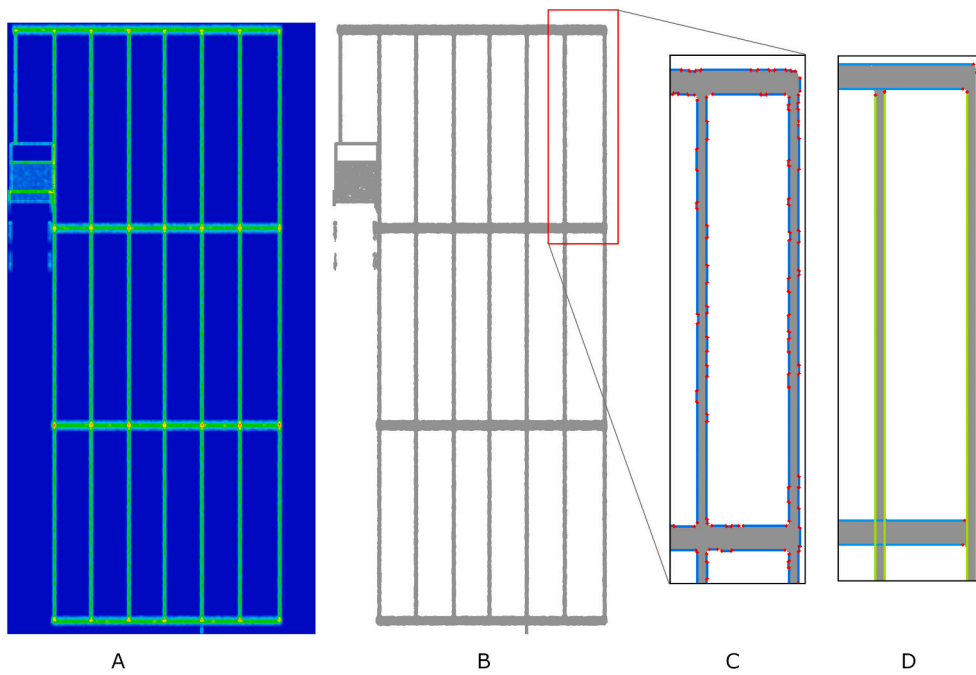


**Fig. 10.** Hough transform beam location process: (A) raw point heatmap, colorized for visualization; (B) binary threshold, (C) line segments (blue) and segment end points (red) from edge detection and Hough transform. (D) beam edge segments after merging, and divided by primary (cyan) and secondary (green) beam layers. Note the initial lack of overlapping at T-connections. (For interpretation of the references to colour in this figure legend, the reader is referred to the web version of this article.)

edge of the beam given the above parameters. From here, the edge pixels were detected using the Canny algorithm [78], which is generally resistant to noise, and converted into line segments using the probabilistic Hough transform [79], finding segments of minimum 40 mm, with a maximum gap of 15 mm.

The segments were divided by their general trend along the X- or Y-axes. For each axis, the total collection of segments was recursively joined by matching segments with nearby endpoints, until each segment represented one edge of a beam.

The system then attempted to match each segment with another segment nearby along its perpendicular axis. Pairs of successfully matched elements were considered the bounds for unique beam objects. While this determined the width of the beam, the length was not yet

accurate (Fig. 10, D) in connection cases where the beams' footprints overlapped. To account for this, the intersection points were found between the centerlines of all beams. If the endpoint of beam was within 200 mm of its theoretical intersection with another beam, the difference was considered an error and the beam was extended. The complete Hough transform step is described in Algorithm 2 in the appendix.

### 3.7. Column detection

After each beam layer was reconstructed, its surrounding region was checked for the presence of supporting columns. Initially, a slice of the raw point cloud was taken 0.5 m below the beam layer. The resulting subcloud was flattened, and clustering applied using the Density-Based
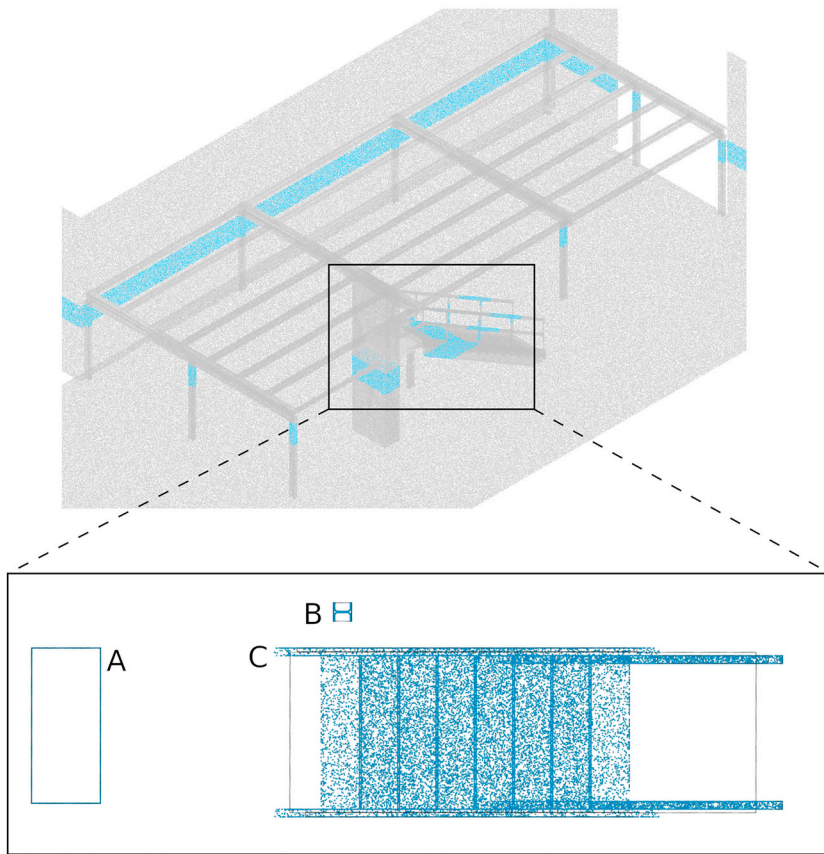
Spatial Clustering of Applications with Noise (DBSCAN) method in order to find candidate locations (Fig. 11). DBSCAN was chosen as the number of clusters (columns) is unknown beforehand, and common column profiles that are searched for in the flattened data may include concave but contiguous regions [80].

The maximum extent (bounding box) of each candidate cluster was then considered. Clusters with bounds below 500 mm on a side and with an aspect ratio smaller than 2/1 were considered legitimate column locations. The columns' bounds were then set using the previously determined floor and beam system heights for the area. Finally, each candidate column was checked to ensure that it intersected a previously found beam. The complete column detection step is described in Algorithm 3 in the appendix.

## 3.8. BIM system modeling

The preceding reconstruction steps established the positions and extents of each element, without relation to the rest of the system. To determine these relationships, the beams were first split, if necessary, and then checked for connections at their ends. Subsequently, to facilitate recovery decisions, the beam system and its building logic were represented as a directed acyclic graph (DAG), being a series of nodes
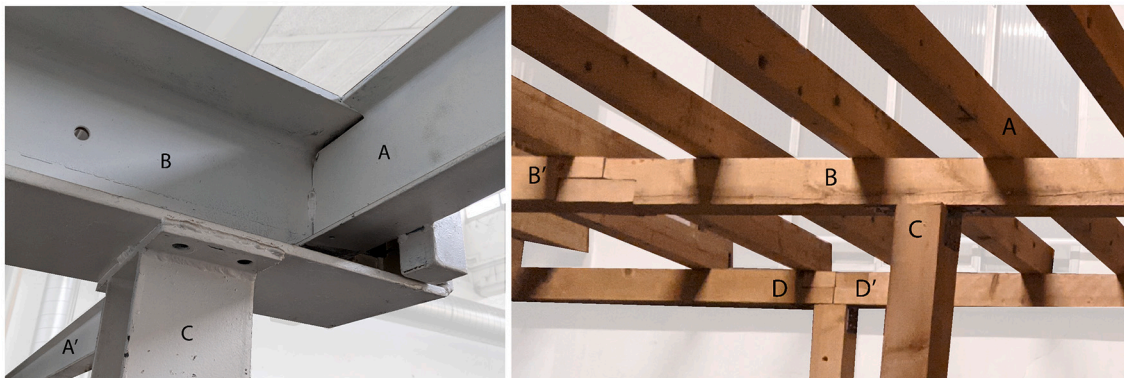


**Fig. 12.** Connection relations in test area (left). Beams A and A' abut and are dependent on beam B, which is in turn dependent on column C. Various abutting and dependency scenarios may be described with this strategy (right), but were not included in this study.
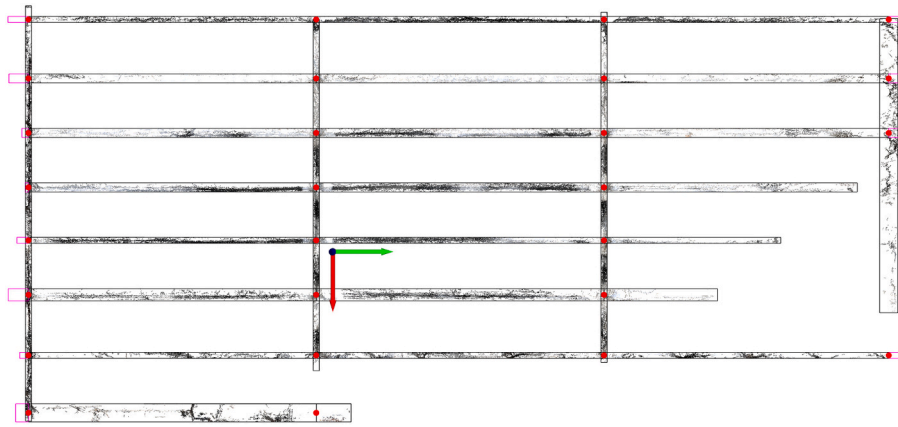
**Fig. 13.** Still image photogrammetry beam system after splitting (split points indicated in red). Resulting beams below a threshold (magenta) were rejected. (For interpretation of the references to colour in this figure legend, the reader is referred to the web version of this article.)

(BIM elements) connected by directed edges (BIM relationships) (Fig. 14). This graph followed the Elemental Graph Data Model [71], indicating which elements were supporting others and informing the order of removal and level of complication.

The analysis supports systems of beams logically divisible into multiple perpendicular layers that support each other. As connection methods may vary, a heuristic was used wherein the direction with a smaller mean distance between beams was assumed to be the secondary layer. In the test area, secondary beams abutted the primary layer instead of sitting on top of it, requiring splitting (Fig. 12, A–A').

During analysis, the mean height of each layer was compared to

determine whether beams abutted and thus required splitting for accurate beam counts and element size estimations. When splitting was necessary, intersections were found between the center lines of each beam. If an intersection point was within a threshold of the ends of a secondary beam, it was assumed to be a correct connection and left in place. In this case, the threshold was set at 100 mm, set by the order of magnitude of the detected beam widths on the site. Alternatively, points located further from the end were assumed to be split points, and two new beams created on either side of the point. This process was repeated until all intersections were resolved (Fig. 13).

At this stage, errors in capture become evident, such as the floating



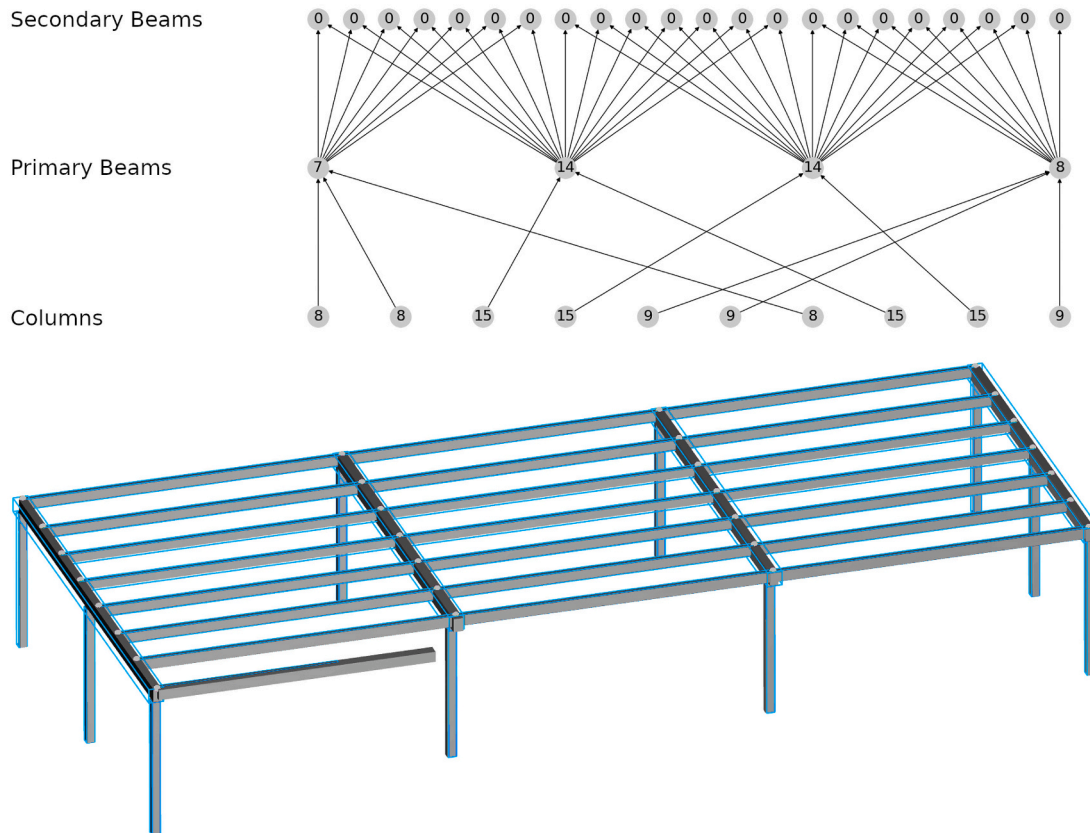**Fig. 14.** (Above) Resulting directed acyclic graph from reconstructed beam system (ground truth cloud), with the recoverability complexity marked, indicating structural dependency and number of downstream elements dependent on each element. (Below) diagram of the reconstructed beam system (gray) compared to ground truth (cyan wire frame). As there are no missing beams or intersections, the graph is accurate for the scene.

beams present on the right of Fig. 13. These were resolved using the extension method described in Section *3.6.2*.

Once all intersections were finalized, each member of the columns, primary beams, and secondary beams sets were assigned a vertex in the vertex sets $V_1$, $V_2$, and $V_3$, respectively, of a multipartite graph $D$ (Fig. 14). Each graph vertex had an associated solid $S$, where $S$ is the bounding box of its associated element geometry; that is,

$$S(i, v \in V_i) \subseteq \mathbb{R}^3.$$

The full graph was defined by the combined bi-adjacency matrices,

$$A_D = \begin{pmatrix} 0_{|V_1|,|V_1|} & B^{12} & B^{13} \\ 0_{|V_2|,|V_1|} & 0_{|V_2|,|V_2|} & B^{23} \\ 0_{|V_3|,|V_1|} & 0_{|V_3|,|V_2|} & 0_{|V_3|,|V_3|} \end{pmatrix},$$

with each individual bi-adjacency matrix position determined by the presence of a solid intersection between members of the sets; that is,

$$B^{kl} = \begin{bmatrix} b_{ij} \end{bmatrix} = \begin{cases} 1, S(k,i) \cap S(l,j) \neq \varnothing \\ 0, otherwise \end{cases}, \forall i \in V_k, \forall j \in V_l$$

For each node/element, a recoverability complexity RC($u$) was calculated for each element $u$. Being the total number of reachable vertices from the element's vertex, RC indicated how many other elements would need to be removed before the element could be recovered. The RC was based on a precomputed reachability matrix $R_D$[81]:

$$R_D = \begin{bmatrix} r_{ij} \end{bmatrix} = \begin{cases} 1, i\ can\ reach\ j\ in\ D \\ 0, otherwise \end{cases}, \forall i \in V(D), \forall j \in V(D)$$

$$RC(i) = \sum_{j \in V_D} R_D[i,j]$$

## 4. Results

The primary results of the process were the reconstructed elements, their individual properties, and resulting graph and RC value. These were considered in light of the raw properties and accuracy measurements of the point clouds captured by each method.

### 4.1. Comparison of data capture techniques

As a baseline, measurements of each cloud's density and accuracy were recorded (Table 2, Table 3). The following parameters were considered:

1. Raw cloud size, a measure of the level of detail of the capture method and a heuristic for judging the quality of the point cloud. It may indicate an on-average denser capture of points within the space, or a more complete capture with fewer gaps.
2. Cleaned cloud size, point count after cleaning operations performed in Section 3.4, but before subsampling. It is an indicator of the level of noise in the method.
3. Capture time, the total duration required by operators to obtain data for a given area of the site. This is affected by the time required to

**Table 3**
Accuracy measuring total distance to ground truth cloud.

| Capture method | Software method | Chamfer distance |
|---|---|---|
| Still image photogrammetry | Metashape | 293.84 |
| 360 video photogrammetry | Metashape | 132.81 |
| Mobile device Lidar | 3D Scanner App | 448.62 |
| | Polycam | 576.23 |
| | Pix4DCatch | 227.74 |

take a single measurement, the method's time between measurements, and the ease of movement with the hardware.

Several types of issues affected the output quality of each tested method, including noise in point location, missing data, creation of non-existent points, and occlusion of relevant geometry. The raw accuracy of each capture method was measured by comparing each captured cloud to the best possible representation of the geometry in point cloud form. This was found by generating a synthetic point cloud with points at equal density across the mesh of the ground truth BIM model. This method created synthetic clouds with a point count set to match the order of magnitude of the captured cloud. The base accuracy of each capture method was measured using the Chamfer distance (Eq. 1) between the captured cloud (C1) and synthetic cloud (C2), which returns distance approximations useful for comparisons in a computationally efficient manner [82]. Smaller distances between clouds indicate more accurate captures.

$$CD(C_1, C_2) = \frac{\sum_{P_1 \in C_1} \min_{P_2 \in C_2} \|P_1 - P_2\|_2^2}{|C_1|} + \frac{\sum_{P_2 \in C_2} \min_{P_1 \in C_1} \|P_2 - P_1\|_2^2}{|C_2|} \tag{1}$$

### 4.2. Element reconstruction

As the reconstructed model's likely use would include supplying data for deconstruction planning, recovery operations, and connecting to new users, errors in the quantity and dimensions of reconstructed elements could affect the viability of recovery, transport, and storage operations, as well as connecting components to new design uses.

The output of each methodology was compared to the ground truth BIM model based on several factors, both relative to the element and absolute within the overall model (Table 4). The total count of predicted elements for each type was compared first. Then, for each predicted element, element position and dimensions were compared to the closest ground truth element by length, difference in cross section size, and finally by cross section offset. The sum of recoverability complexity measurements between all detected elements was also compared to the ground truth model.

## 5. Discussion

The complete set of evaluated methods for the proposed procedure is shown in Fig. 15. The methods in sections 3.2–3.4 all required some

**Table 2**
Operator time and output size for the test capture methods.

| Capture method | Raw cloud size | Cleaned cloud size | Capture time |
|---|---|---|---|
| Still image photogrammetry | 26,466,370 | 16,778,419 | 08:00 |
| 360 video photogrammetry | 27,190,095 | 7,134,258 | 01:00 |
| Lidar 1 | 11,288,843 | 7,764,338 | 05:00 |
| Lidar 2 | 491,373 | 393,299 | 10:00 |
| Lidar 3 | 469,646 | 440,488 | 10:00 |

**Table 4**
Comparison of reconstructed geometry to ground truth geometry. Lowest error for each factor is indicated in bold.

| Capture method | Analysis Method | Element count difference | | Median length difference (mm) | | Median cross section difference (mm) | | Median cross section offset (mm) | | TRC | TRC error |
|---|---|---|---|---|---|---|---|---|---|---|---|
| | | C (10) | B (26) | C | B | C | B | C | B | | |
| Synthetic point cloud | *P* | 0 | 0 | 10.9 | 19.3 | 44.1 | 25.9 | 2.0 | 7.3 | 154 | **0** |
| | *T* | 0 | 0 | 8.5 | 30.6 | 47.0 | 26.0 | 4.2 | 8.0 | 136 | 18 |
| Stationary photogrammetry | *P* | −6 | **0** | 42.6 | 588.2 | 37.6 | **57.9** | 102.2 | **36.0** | 61 | 93 |
| | *T* | −5 | 4 | 60.7 | 456.9 | **37.2** | 331.0 | **102.1** | 72.3 | 72 | 82 |
| 360 video photogrammetry | *P* | −4 | −2 | 72.6 | **40.0** | 46.3 | 114.0 | 130.1 | 44.7 | 81 | 73 |
| | *T* | **−1** | 6 | 70.2 | 43.5 | 55.4 | 278.9 | 167.9 | 73.4 | 113 | **41** |
| Lidar 1 | *P* | −6 | 7 | 336.4 | 1968.7 | 59.9 | 137.97 | 181.0 | 188.7 | 54 | 100 |
| | *T* | −7 | 17 | 51.87 | 536.49 | 49.61 | 433.0 | 260.0 | 105.1 | 34 | 120 |
| Lidar 2 | *P* | −8 | 9 | 107.7 | 2807.4 | 80.5 | 106.58 | 588.15 | 26.9 | 72 | 82 |
| | *T* | −7 | **0** | 191.5 | 4170.0 | 107.46 | 426.0 | 937.7 | 265.5 | 58 | 96 |
| Lidar 3 | *P* | −4 | −6 | **36.8** | 896.6 | 51.7 | 63.6 | 149.6 | 75.6 | 65 | 89 |
| | *T* | −4 | −9 | 41.2 | 1399.7 | 66.0 | 200.0 | 135.1 | 97.9 | **28** | 126 |
| | **C**olumn [C]; **B**eam [B]; | | | | | | | | | | |
| | Histogram **P**eak Method [P]; Hough **T**ransform Method [T]; | | | | | | | | | | |
| | **T**otal **R**ecoverability **C**omplexity [TRC] | | | | | | | | | | |
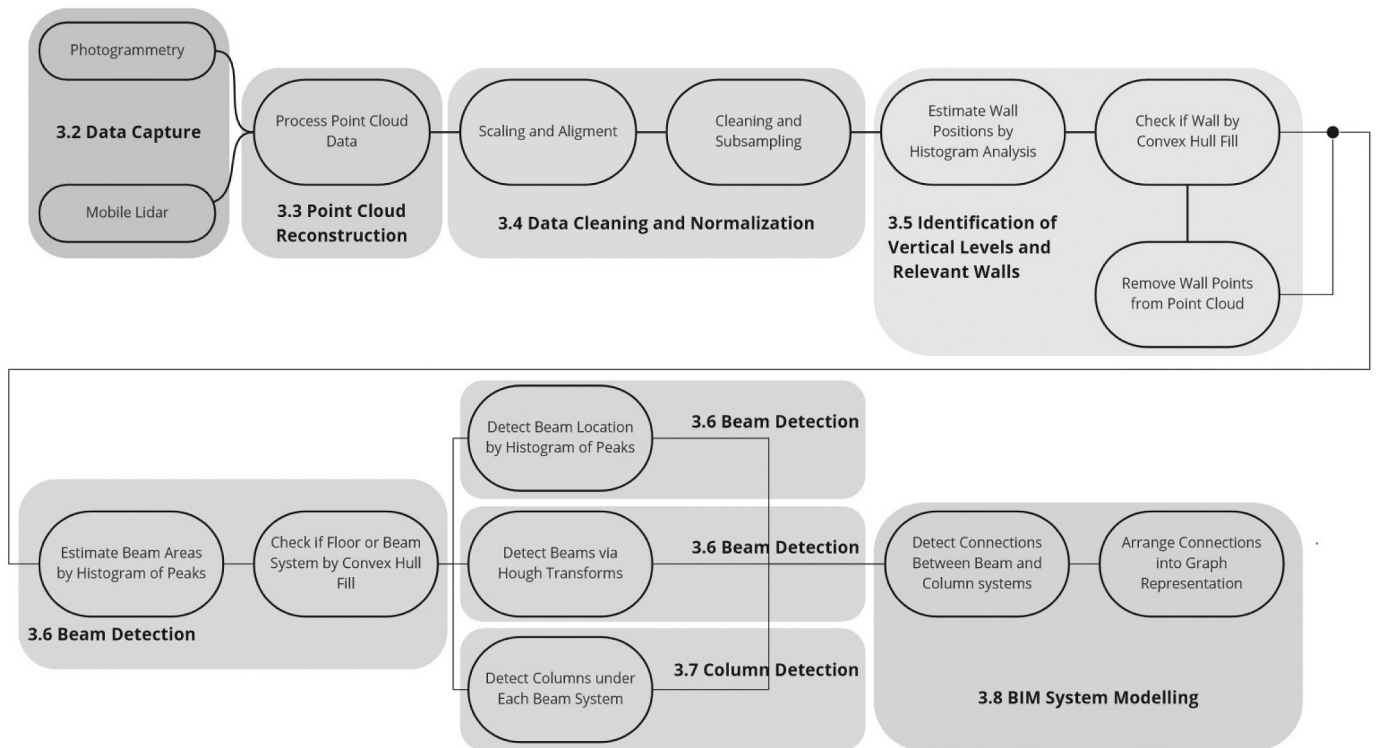


**Fig. 15.** Overview of analysis steps with methods applied, listed by section number in methods section.

degree of manual operation, while the methods described in sections 3.5–3.8 form an automated pipeline. With regard to testing capture methods, all hand-directed methods took similar amounts of time and required constant operator attention to capture useful data.

The worst-case length errors observed in the case study are indicative of the cumulative effects of missed elements. For example, in the case of Lidar 2, a primary beam was missed due to appearing weakly in the in-app reconstruction, leading to oversized reconstruction of the attached secondary beams. Similarly, false-positive primary beams (such as in Lidar 1), over-split and undersized the secondary layer. Less extreme but persistent errors, such as the mismatch in length between similar elements, stem from gaps in reconstruction. This indicates the possible application of domain-specific error-checking methods.

While methods were developed to mitigate noise and incorrectly reconstructed features, missing data proved a larger source of error. This included gaps in flat surfaces during Lidar scanning or geometry ending before its full extent due to a lack of accessible photography angles. At worst, this prevented from being able to discern between floors and beam layers, or the identification of walls for point cleaning. While extending short elements can be predicted (such as with columns), this runs the risk of overextending to non-related elements. These types of issues may be addressable by the inclusion of a whole-model pass to decide which elements are likely to be legitimate based on context. Additionally, given the challenges of overcoming missing data at the BIM level, this indicates to the usefulness of hole-filling and data prediction tools at the original point cloud stage.

The varied effects of different types of capture error were also reflected when comparing the Chamfer distance to the reconstruction results. In many categories, the amount of error between methods does not linearly reflect the difference in cloud error measured by the Chamfer distance. Each analysis method is resistant to the noise characteristics of the capture methods in different ways, aside from the pure per-point distance error.

Given the cumulative effects of these intrinsic error types on the procedure outcomes, mobile device Lidar is not presently considered viable for steel-structure BIM reconstruction at this scale. However, as data from mobile Lidar undergoes heavy processing on the device before being returned to the use, off-the-shelf apps for interfacing with the scan hardware may simply be non-domain specific, and a purpose-built interface may be necessary. The photogrammetry methods had similar results under most metrics, though the still image photogrammetry showed worse outliers.

Under idealized capture circumstances (represented by the synthetic dataset), the histogram peak method was found to perform better than the Hough transform method. Although this was not always consistent across some metrics for the physical scanning methods, it is still considered the most viable option. However, in this case the methods were tested in isolation, and a combination may allow each method to account for the errors of the other.

BIM relationship analysis provides a numerical means of judging recoverability; however, its effects on generalizability are not immediately clear. Given the high variation and customized solutions in construction, unusual elements or assembly methods may be ignored or incorrectly assessed by a particular set of BIM relationship rules. In this context, the 360-video photogrammetry again showed itself to be the most accurate of the real capture methods. Measuring the total difference between the sum of complexities put the greatest importance on correctly connected columns, as each would have the most downstream elements.

The errors across all methods highlighted the challenges for reconstruction systems when working with the particular capture artifacts of steel structural components. This remains a necessary expansion of the well-studied case of concrete structural elements, as the reuse potential of these construction systems is low [83] and more research on recovery techniques is needed. Additionally, as this study focused on the particular case of components stocked in obsolete buildings or in buildings that will become available for reuse in the near future, this research did not consider existing damaged components exposed to unforeseen events such as fires or earthquakes. The materials subjected to unforeseen events present more challenges for reuse in their current state [83] and are more likely to fit within recycling processes that do not require explicit BIM reconstruction.

## 6. Future research

This methodology covered the essential types of data needed to communicate about material stocks between different actors. Further research would produce more in-depth per-element data. For instance, for steel elements, predictions about specific profile dimensions, even in cases of point cloud occlusion and low point density, would allow for more informed decisions regarding the element's structural capabilities. The abundance of image data collected for each element would allow for initial computer vision-based predictions about possible damage or decay. Computer vision techniques could also facilitate for the

integration of existing techniques for reconstruction concrete structural components by delineating areas of differing materials and allowing for the analysis of hybrid steel and reinforced concrete structures.

Recovery scoring would be enhanced by the additional reconstruction of connection details. Currently the system treats all connections as equal and considers each as a single removal operation. However, a combination of geometric and image analyses could differentiate between, for example, bolted and welded connections.

Additional robustness would be ensured by evaluating these techniques in a variety of environmental conditions. In this study, the recovery location was indoors, with a combination of artificial and diffused natural light. There was little glass or other reflective materials in the critical area, whose presence would induce different types of noise in the captured data.

Given the strong effects of the different varieties of noise generated by the various capture methods, generalizability would be improved by being able to test against a large number of synthetic sites, utilizing noise-application techniques developed for sim-to-real applications in order to mimic a variety of capture methods.

This work specifically built on low-cost or consumer-grade scanning tools, with an inherent tradeoff between user accessibility and data quality in comparison to terrestrial Lidar systems. Testing with a broader set of scanning methods against the same reconstruction methods would make this tradeoff explicitly measurable in the domain.

Presently, this pipeline produces geometry and associated information in an internal format. For further practical use, export into an open format such as Industry Foundation Classes (IFC), would be necessary. Additionally, the original point cloud data forming each element may be a valuable source of information for future users to apply their own analysis, and could be included efficiently in the final output with contemporary BIM-point cloud integration techniques [84].

Finally, beyond data and geometric format, analysis via BIM will be affected by the choice of building-domain paradigm used. There are several contemporary standards for BIM classes and relationships between different countries, companies, and researchers. Choice of BIM paradigm will affect both the details of the analysis performed as well as its applicability for recoverability analysis.

## 7. Conclusions

This case study demonstrates how site data captured with accessible technology can support the digitization of steel structural building stocks for circularity purposes. Specifically, this technology would be positioned as a first step to generate digital information for use in all future communication and design steps.

The study is part of ongoing research in the field of Scan-to-BIM methods, focusing on existing building stocks and reconstructing inter-element relationships. The case study focuses on adapting existing Scan-to-BIM processes to create digital models of demolition sites, to better plan for deconstruction works, and to derive more value from the recovered materials. This is built on a data capture process assuming low-cost hardware viable for wide adoption in industry.

The implemented Scan-to-BIM process builds on existing reconstruction methods by specifically focusing on the BIM classes for steel column and beam systems, chosen for their direct usability as recoverable elements. Specifically, these component types present challenges for accurate capture and are less commonly studied in contemporary Scan-to-BIM research. The nature of these elements also necessitates the

reconstruction of element relationships in addition to volumetric and geometric data, as well as modeling methods for considering all interconnections of a site. This analysis is necessary for uncovering possible obstacles to recovery when implementing circularity on a site built with linear thinking. The study showed the feasibility of automated reconstruction in relation to structural elements while highlighting the strong effects of data capture noise on the accuracy of the results.

The project also demonstrates the state of accessible technologies, such as mobile devices, for capturing reliable information for deconstruction purposes. Low-cost 360-degree cameras proved the most viable with respect to noise and accuracy for this procedure, while mobile Lidar systems would require additional domain-specific development. The continuing development of this technology is necessary for a viable integration of digital solutions into current workflows with minimal disruption.

Ultimately, Scan-to-BIM tools form the logistical base for a complex reuse analysis. Transforming unstructured data into standardized classes and relationships helps additional actors in the field conduct economic and logistical analysis. This information can then facilitate connections between circular economy actors in the larger ecosystem of inventory, logistics, and matching tools.

## Funding

## Declaration of Competing Interest

The authors declare the following financial interests/personal relationships which may be considered as potential competing interests:

Matthew Gordon reports financial support was provided by Vlaanderen Circulair. Matthew Gordon reports administrative support was provided by Materiuum. Matthew Gordon reports administrative support was provided by Anku. Matthew Gordon reports writing assistance was provided by MIT Writing and Communication Center. Matthew Gordon reports a relationship with Scaled Robotics that includes: employment.

## Data availability

Source code for described procedure is linked in article. Authors do not currently have permission to share other data.

### Acknowledgments

### Source

Source code for the methods described can be found at: https://github.com/cea-ethz/beam_system_reconstruction.

## Appendix: Pseudocode for detection algorithms

**Algorithm 1**. Pseudocode for finding beam systems in an arbitrary point cloud.

```
Data: point cloud C with coordinates in mm
Result: list of z values beam_layers, z value of floor_height
bin_count = (max(C.z) – min(C.z)) / 50
bins = histogram of C with bin_count bins
smooth_bins = for each bin_i in bins:
        smooth_bin_i = bin_i + bin_{i-1} + bin_{i+1}
smooth_bins = smooth_bins / sum(smooth_bins)
peaks = peaks of smooth_bins given prominence, width, relative_height
for each peak_i in peaks:
        slice = points of C in bin_i
        slice_2d = [point.x point.y] for each point in slice
        image_a = |set(int(slice_2d / 40))| * 40
        image_b = |set(int(slice_2d / 200))| * 200
        if image_a / image_b < tuned cutoff (0.5)
                add (i * 50) to beam_layers
        else:
                floor_height = i * 50
```

**Algorithm 2.** Pseudocode for Hough transform-based beam detection.

---

**Data:** Point cloud *C* in mm, being the slice of the previously found beam layer
**Result:** list of beams *beams_x_axis* and list of beams *beams_y_axis*
scale C by 1/scale_factor
round point positions of *C* to integers
*image* = array of zeroes with dimensions of *cloud* bounds width and height, divided by *scale_factor*
**for each** *point* in *C:*
    add 1 to the subset of *image* from ($point.x - 5$, $point.y - 5$) to ($point.x + 5$, $point.y + 5$)

apply threshold operation to *image* with tuned cutoff variable (22)
apply canny edge detection to *image*

*lines* = array of line segments from the probabilistic hough transform of *image*

divide *lines* into new lists *lines_h* and *lines_v* such that:
    **if** ratio of width(*line*) to height*(line)* > 5:
        add *line* to *lines_h*
    **if** ratio of height(*line)* to height(*line)* > 5:
        add *line* to *lines_v*

*lines_h* = join_lines(*lines_h*)
*lines_v* = join_lines(*lines_v*)

*clusters_h* = cluster_lines(*lines_h*)
*clusters_v* = cluster_lines(*lines_v*)

**for each** cluster in clusters_h
    add *beam* to *beams_x_axis* being the bounding box of *cluster*
**for each** cluster in clusters_v
    add *beam* to *beams_y_axis* being the bounding box of *cluster*

**return** beams_x_axis and beams_y_axis




**function** join_lines:
**Data**: list of line segments *lines*
**Result**: list of line segments
**repeat** until no joins are performed:
    **for each** *line_a* in lines:
        **for each** *line_b* in lines that is not *line_a*:
            **if** perpendicular distance between centerpoints of *line_a* and *line_b* < 10mm:
                remove line_a and line_b from *lines*
                add new line from start of *line_a* to end of *line_b* to *lines*
                break to outer repeat
**return** lines


**function** cluster_lines:
**Data**: list of line segments *lines*
**Result**: list of lists of lines
*clusters* is an empty list
sort *lines* by descending length
**for each** line in lines:
    **for each** cluster in clusters:
        **if** perpendicular distance from *line* centerpoint to *cluster* centerpoint < 50mm:
            add *line* to *cluster*
    **if** *line* was added to no *cluster*:
        add line to new_cluster
        add new_cluster to clusters
**return** clusters

---

**Algorithm 3.** Pseudocode for column detection.

```
Data:
Point cloud C in mm, being the slice below the previously found beam layer in the Z axis
list of beams from previous step
floor_height from previous step
Result: list of columns

flatten C to XY plane
subclouds = DBSCAN clustering of C
for each subcloud in subclouds:
    if x range and y range of subcloud are both between 60mm and 500mm:
        for each beam in beams:
            if bounding_box of subcloud intersects bounding box of beam:
                column is a new column with bounding_box of subcloud, with Z extents from -
                floor_height to minimum Z of bounding box of beam
                add column to columns
return columns
```

## References

[1] UNECE, Share of Construction in GDP - Data Portal - United Nations Economic Commission for Europe, UNECE, 2021. https://w3.unece.org/PXWeb/en/CountryRanking?IndicatorCode=8 (accessed Nov. 21, 2022).

[2] World Economic Forum, "Shaping the Future of Construction: A Breakthrough in Mindset and Technology," World Economic Forum, Accessed: Feb. 03, 2022. [Online]. Available: https://www.weforum.org/reports/shaping-the-future-of-construction-a-breakthrough-in-mindset-and-technology/, May 2016.

[3] S. Giljum, H. Wieland, S. Lutter, M. Bruckner, R. Wood, A. Tukker, K. Stadler, Identifying priority areas for European resource policies: a MRIO-based material footprint assessment, J. Econ. Struct. 5 (1) (Dec. 2016) 17, https://doi.org/10.1186/s40008-016-0048-5.

[4] Eurostat, Generation of waste by waste category, hazardousness and NACE Rev. 2 activity. https://ec.europa.eu/eurostat/databrowser/view/env_wasgen/default/table?lang=en, 2018 (accessed Feb. 09, 2022).

[5] Directive 2008/98/EC of the European Parliament and of the Council of 19 November 2008 on waste and repealing certain Directives (Text with EEA relevance), Accessed: Aug. 28, 2022. [Online]. Available, http://data.europa.eu/eli/dir/2008/98/2018-07-05/eng, 2018.

[6] European Commission, Report from the Commission to the European Parliament, the Council, the European Economic and Social Committee and the Committee of the Regions on the Implementation of EU Waste Legislation, Including the Early Warning Report for Member States at Risk of Missing the 2020 Preparation for Re-use/Recycling Target on Municipal Waste, Accessed: Feb. 01, 2022. [Online]. Available, https://eur-lex.europa.eu/legal-content/EN/TXT/?qid=1537873850842&uri=COM:2018:656:FIN, 2018.

[7] European Commission, Communication from the commission to the european parliament, the council, the european economic and social committee and the committee of the regions - Environmental Implementation Review 2022 - Turning the tide through environmental compliance, Accessed: Oct. 19, 2022. [Online]. Available, https://eur-lex.europa.eu/legal-content/EN/ALL/?uri=comnat:COM_2022_0438_FIN, 2022.

[8] A. Di Maria, J. Eyckmans, K. Van Acker, Downcycling versus recycling of construction and demolition waste: combining LCA and LCC to support sustainable policy making, Waste Manag. 75 (May 2018) 3–21, https://doi.org/10.1016/j.wasman.2018.01.028.

[9] Eurostat, Eurostat - Data Explorer - Circular material use rate. http://appsso.eurostat.ec.europa.eu/nui/show.do?dataset=cei_srm030&lang=en, 2020 (accessed Feb. 01, 2022).

[10] J. Kirchherr, D. Reike, M. Hekkert, Conceptualizing the circular economy: an analysis of 114 definitions, Resour. Conserv. Recycl. 127 (Dec. 2017) 221–232, https://doi.org/10.1016/j.resconrec.2017.09.005.

[11] N. Heeren, S. Hellweg, Tracking construction material over space and time: prospective and geo-referenced modeling of building stocks and construction material flows, J. Ind. Ecol. 23 (1) (2019) 253–267, https://doi.org/10.1111/jiec.12739.

[12] J. Hart, K. Adams, J. Giesekam, D.D. Tingley, F. Pomponi, Barriers and drivers in a circular economy: the case of the built environment, Procedia CIRP 80 (Jan. 2019) 619–624, https://doi.org/10.1016/j.procir.2018.12.015.

[13] S. Çetin, C. De Wolf, N. Bocken, Circular digital built environment: an emerging framework, Sustainability 13 (11) (Jun. 2021) 6348, https://doi.org/10.3390/su13116348.

[14] V. Burrows, E. Watson, Advancing Net Zero Whole Life Carbon, World Green Building Council, Sep. 2021. Accessed: Feb. 01, 2022. [Online]. Available: https://worldgbc.org/advancing-net-zero/advancing-net-zero-whole-life-carbon/.

[15] UNFCCC, Glasgow Climate Pact, Accessed: Feb. 08, 2022. [online]. Available, https://unfccc.int/sites/default/files/resource/cma2021_L16_adv.pdf, 2021.

[16] R. Jin, K. Panuwatwanich, Z. Adamu, U. Madanayake, O.J. Ebohon, Developing a methodological framework for adopting digitalization for deconstruction planning, Am. Inst. Phys. Conf. Proc. 2428 (1) (Nov. 2021), 030001, https://doi.org/10.1063/5.0071722.

[17] J. Potting, M. Hekkert, E. Worrell, A. Hanemaaijer, Circular Economy: Measuring Innovation in Product Chains, PBL Netherlands Environmental Assessment Agency, Jan. 24 2017. https://www.pbl.nl/en/publications/circular-economy-measuring-innovation-in-product-chains (accessed Aug. 20, 2022).

[18] Directorate-General for Research and Innovation (European Commission), C. Schempp, P. Hirsch, Categorisation System for the Circular Economy: A Sector Agnostic Categorisation System for Activities Substantially Contributing to the Circular Economy, LU: Publications Office of the European Union, 2020 (ISBN: 978-92-76-10527-5).

[19] Building Material Scout, BMS - Building Material Scout, BMS - Building Material Scout, 2022. https://building-material-scout.com (accessed Feb. 09, 2022).

[20] zirkular. https://zirkular.net/, 2022 (accessed Oct. 26, 2022).

[21] Opalis, Homepage | Opalis. https://opalis.eu/en, 2022 (accessed Feb. 08, 2022).

[22] M. Heinrich, W. Lang, "Material passports - Best practice," Buildings as Material Banks, ISBN: 978–3–941370-96-8, 2019.

[23] useagain, Plattform für Bauteil-Wiederverwendung, in: useagain, 2022. https://www.useagain.ch/de/ (accessed Oct. 26, 2022).

[24] Enviromate, Enviromate | Free Leftover Building Materials Marketplace. https://www.enviromate.co.uk/, 2020 (accessed Feb. 08, 2022).

[25] Excess Materials Exchange, Excess Materials Exchange. https://excessmaterialsexchange.com/en_us/, 2022 (accessed Feb. 08, 2022).

[26] New Horizon, "New Horizon," New Horizon. https://newhorizon.nl/, 2022 (accessed Feb. 08, 2022).

[27] Rotor Deconstruction, Rotor Deconstruction – Reuse of Building Materials Made Easy. https://rotordc.com/, 2022.

[28] Materiuum, materiuum – Association créative. https://materiuum.ch/, 2022 (accessed Feb. 08, 2022).

[29] P. Gerbert, S. Castagnino, C. Rothballer, A. Renz, R. Filitz, The Transformative Power of Building Information Modeling, Boston Consulting Group, Mar. 2016. Accessed: Mar. 17, 2022. [Online]. Available: https://www.bcg.com/publications/2016/engineered-products-infrastructure-digital-transformative-power-building-information-modeling.

[30] European Commission, New European Bauhaus, European Commission, 2021. https://europa.eu/new-european-bauhaus/about/delivery_en (accessed Jan. 30, 2022).

[31] F. Chiabrando, G. Sammartano, A. Spano, Historical buildings models and their handling via 3d survey: From points clouds to user-oriented hbim, in: ISPRS - International Archives of the Photogrammetry, Remote Sensing and Spatial Information Sciences XLI-B5, Jun. 2016, pp. 633–640, https://doi.org/10.5194/isprs-archives-XLI-B5-633-2016.

[32] P. Tang, D. Huber, B. Akinci, R. Lipman, A. Lytle, Automatic reconstruction of as-built building information models from laser-scanned point clouds: a review of related techniques, Autom. Constr. 19 (7) (Nov. 2010) 829–843, https://doi.org/10.1016/j.autcon.2010.06.007.

[33] Q. Wang, M.-K. Kim, Applications of 3D point cloud data in the construction industry: a fifteen-year review from 2004 to 2018, Adv. Eng. Inform. 39 (Jan. 2019) 306–319, https://doi.org/10.1016/j.aei.2019.02.007.

[34] S. Xu, J. Wang, W. Shou, T. Ngo, A.-M. Sadick, X. Wang, Computer vision techniques in construction: a critical review, Arch. Comput. Methods Eng. 28 (5) (Aug. 2021) 3383–3397, https://doi.org/10.1007/s11831-020-09504-3.

[35] F. Bosché, M. Ahmed, Y. Turkan, C.T. Haas, R. Haas, The value of integrating scan-to-BIM and scan-vs-BIM techniques for construction monitoring using laser scanning and BIM: the case of cylindrical MEP components, Autom. Constr. 49 (Jan. 2015) 201–213, https://doi.org/10.1016/j.autcon.2014.05.014.

[36] E. Valero, D.D. Mohanty, M. Ceklarz, B. Tao, F. Bosche, G.I. Giannakis, S. Fenz, K. Katsigarakis, G.N. Lilis, D. Rovas, A. Papanikolaou, An Integrated Scan-to-BIM Approach for Buildings Energy Performance Evaluation and Retrofitting, in: Proceedings of the 38th International Symposium on Automation and Robotics in Construction, Nov. 2021, pp. 204–211, https://doi.org/10.22260/ISARC2021/0030.

[37] G. Luetzenburg, A. Kroon, A.A. Bjørk, Evaluation of the apple iPhone 12 pro LiDAR for an application in geosciences, Sci. Rep. 11 (1) (Nov. 2021), https://doi.org/10.1038/s41598-021-01763-9. Art. no. 1.

[38] A. Riquelme, R. Tomás, M. Cano, J.L. Pastor, L. Jordá-Bordehore, Extraction of discontinuity sets of rocky slopes using iPhone-12 derived 3DPC and comparison to TLS and SfM datasets, IOP Conf. Series Earth Environ. Sci. 833 (1) (Aug. 2021), 012056, https://doi.org/10.1088/1755-1315/833/1/012056.

[39] P. Subramanian, M. Gheisari, Using 360-Degree Panoramic Photogrammetry and Laser Scanning Techniques to Create Point Cloud Data: A Comparative Pilot Study, in: Associated Schools of Construction International Proceedings of the Annual Conference, Apr. 2019, pp. 743–750. Accessed: Jan. 30, 2022. [Online]. Available, http://ascpro0.ascweb.org/archives/cd/2019/paper/CPRT305002019.pdf.

[40] F. Yilmazturk, A.E. Gurbak, Geometric evaluation of Mobile-phone camera images for 3D information, Int. J. Optics Sep. 2019 (2019), e8561380, https://doi.org/10.1155/2019/8561380.

[41] M. Yeh, T.-Y. Chou, L. Yang, The Evaluation of GPS techniques for UAV-based Photogrammetry in Urban Area, in: ISPRS - International Archives of the Photogrammetry, Remote Sensing and Spatial Information Sciences XLI-B1, Jun. 2016, pp. 1079–1084, https://doi.org/10.5194/isprsarchives-XLI-B1-1079-2016.

[42] Z.P.L. Tungol, H. Toriya, N. Owada, I. Kitahara, F. Inagaki, M. Saadat, H.D. Jang, Y. Kawamura, Model scaling in smartphone GNSS-aided photogrammetry for fragmentation size distribution estimation, Minerals 11 (12) (Dec. 2021), https://doi.org/10.3390/min11121301. Art. no. 12.

[43] J.M. Coughlan, A.L. Yuille, The Manhattan world assumption: regularities in scene statistics which enable Bayesian inference, in: *Proceedings of the 13th International Conference on Neural Information Processing Systems*, Cambridge, MA, USA, Jan. 2000, pp. 809–815. Accessed: Nov. 21, 2022. [Online]. Available, https://proceedings.neurips.cc/paper/2000/hash/90e1357833654983612fb05e3ec9148c-Abstract.html. ISBN: 978–0–262-52651-7.

[44] J. Straub, G. Rosman, O. Freifeld, J.J. Leonard, J.W. Fisher, A Mixture of Manhattan Frames: Beyond the Manhattan World, in: 2014 IEEE Conference on Computer Vision and Pattern Recognition, Jun. 2014, pp. 3770–3777, https://doi.org/10.1109/CVPR.2014.488.

[45] P. Hübner, M. Weinmann, S. Wursthorn, S. Hinz, "Pose Normalization of Indoor Mapping Datasets Partially Compliant to the Manhattan World Assumption," *arXiv: 2107.07778 [cs]*, Accessed: Jan. 30, 2022. [Online]. Available, http://arxiv.org/abs/2107.07778, Jul. 2021.

[46] I. Coudron, S. Puttemans, T. Goedemé, P. Vandewalle, Semantic extraction of permanent structures for the reconstruction of building interiors from point clouds, Sensors 20 (23) (Jan. 2020), https://doi.org/10.3390/s20236916. Art. no. 23.

[47] C. Emunds, N. Pauen, V. Richter, J. Frisch, C. van Treeck, SpaRSE-BIM: classification of IFC-based geometry via sparse convolutional neural networks, Adv. Eng. Inform. 53 (Aug. 2022), 101641, https://doi.org/10.1016/j.aei.2022.101641.

[48] S. Ochmann, R. Vock, R. Klein, Automatic reconstruction of fully volumetric 3D building models from oriented point clouds, ISPRS J. Photogramm. Remote Sens. 151 (May. 2019) 251–262, https://doi.org/10.1016/j.isprsjprs.2019.03.017.

[49] S. Oesau, F. Lafarge, P. Alliez, Indoor scene reconstruction using feature sensitive primitive extraction and graph-cut, ISPRS J. Photogramm. Remote Sens. 90 (Apr. 2014) 68–82, https://doi.org/10.1016/j.isprsjprs.2014.02.004.

[50] M. Bassier, B. Van Genechten, M. Vergauwen, Classification of sensor independent point cloud data of building objects using random forests, J. Building Eng. 21 (Jan. 2019) 468–477, https://doi.org/10.1016/j.jobe.2018.04.027.

[51] X. Xiong, A. Adan, B. Akinci, D. Huber, Automatic creation of semantically rich 3D building models from laser scanner data, Autom. Constr. 31 (May 2013) 325–337, https://doi.org/10.1016/j.autcon.2012.10.006.

[52] E. Valero, A. Adán, F. Bosché, Semantic 3D reconstruction of furnished interiors using laser scanning and RFID technology, J. Comput. Civ. Eng. 30 (4) (Jul. 2016) 04015053, https://doi.org/10.1061/(ASCE)CP.1943-5487.0000525.

[53] Y.-J. Cha, W. Choi, G. Suh, S. Mahmoudkhani, O. Büyüköztürk, Autonomous structural visual inspection using region-based deep learning for detecting multiple damage types: autonomous SHM using deep faster R-CNN, Computer-Aided Civil Infrastructure Eng. 33 (9) (Sep. 2018) 731–747, https://doi.org/10.1111/mice.12334.

[54] A. Dimitrov, M. Golparvar-Fard, Vision-based material recognition for automated monitoring of construction progress and generating building information modeling from unordered site image collections, Adv. Eng. Inform. 28 (1) (Jan. 2014) 37–49, https://doi.org/10.1016/j.aei.2013.11.002.

[55] K. Xiao, L. Engstrom, A. Ilyas, A. Ma, Noise or signal: The role of image backgrounds in object recognition, in: International Conference of Learning Representations 2021, 2021, p. 28. Accessed: Feb. 16, 2022. [Online]. Available, https://openreview.net/forum?id=gl3D-xY7wLq.

[56] J.L. Iglesias, J.A.D. Severiano, P.E.L. Amorocho, C.M. del Val, V. Gómez-Jáuregui, O.F. García, A.P. Royano, C.O. González, Revision of Automation Methods for Scan to BIM, in: International conference on The Digital Transformation in the Graphic Engineering: Advances in Design Engineering, 2019, pp. 482–490, https://doi.org/10.1007/978-3-030-41200-5_53.

[57] B. Okorn, X. Xiong, B. Akinci, Toward Automated Modeling of Floor Plans, in: Proceedings of the symposium on 3D data processing, visualization and transmission 2, 2010. Accessed: Jan. 30, 2022. [Online]. Available, https://www.semanticscholar.org/paper/Toward-Automated-Modeling-of-Floor-Plans-Okorn-Xiong/3aacae3356e52a12c6e74926a289cc4495bc9bdf.

[58] K. Khoshelham, L. Díaz-Vilariño, 3D Modelling of Interior Spaces: Learning the Language of Indoor Architecture, in: The International Archives of the Photogrammetry, Remote Sensing and Spatial Information Sciences XL–5, Jun. 2014, pp. 321–326, https://doi.org/10.5194/isprsarchives-XL-5-321-2014.

[59] C. Galamhos, J. Matas, J. Kittler, Progressive probabilistic Hough transform for line detection, in: Proceedings. 1999 IEEE Computer Society Conference on Computer Vision and Pattern Recognition (Cat. No PR00149) 1, Jun. 1999, pp. 554–560. Vol. 1, https://doi.org/10.1109/CVPR.1999.786993.

[60] L. Yang, J.C.P. Cheng, Q. Wang, Semi-automated generation of parametric BIM for steel structures based on terrestrial laser scanning data, Autom. Constr. 112 (Apr. 2020), 103037, https://doi.org/10.1016/j.autcon.2019.103037.

[61] Y. Turkan, F. Bosché, C.T. Haas, R. Haas, Tracking of secondary and temporary objects in structural concrete work, Constr. Innov. 14 (2) (2014) 145–167, https://doi.org/10.1108/CI-12-2012-0063.

[62] M. Guo, M. Sun, D. Pan, M. Huang, B. Yan, Y. Zhou, P. Nie, T. Zhou, Y. Zhao, High-precision detection method for large and complex steel structures based on global registration algorithm and automatic point cloud generation, Measurement 172 (Feb. 2021), 108765, https://doi.org/10.1016/j.measurement.2020.108765.

[63] H. Son, C. Kim, Semantic as-built 3D modeling of structural elements of buildings based on local concavity and convexity, Adv. Eng. Inform. 34 (Oct. 2017) 114–124, https://doi.org/10.1016/j.aei.2017.10.001.

[64] Y. Xu, S. Tuttas, L. Hoegner, U. Stilla, Reconstruction of scaffolds from a photogrammetric point cloud of construction sites using a novel 3D local feature descriptor, Autom. Constr. 85 (Jan. 2018) 76–95, https://doi.org/10.1016/j.autcon.2017.09.014.

[65] H. Kim, C. Kim, 3D as-built modeling from incomplete point clouds using connectivity relations, Autom. Constr. 130 (Oct. 2021), 103855, https://doi.org/10.1016/j.autcon.2021.103855.

[66] F. Kaufmann, C. Glock, T. Tschickardt, ScaleBIM: Introducing a scalable modular framework to transfer point clouds into semantically rich building information models, in: Proceedings of the 2022 Conference of European Council for Computing in Construction 3, Jul. 2022, pp. 214–221, https://doi.org/10.35490/EC3.2022.194.

[67] B. Wang, Q. Wang, J.C.P. Cheng, C. Yin, Object verification based on deep learning point feature comparison for scan-to-BIM, Autom. Constr. 142 (Oct. 2022), 104515, https://doi.org/10.1016/j.autcon.2022.104515.

[68] T. Krijnen, M. Tamke, Assessing Implicit Knowledge in BIM Models with Machine Learning, Jan. 2015, pp. 397–406, https://doi.org/10.1007/978-3-319-24208-8_33.

[69] K. Shea, J. Cagan, Languages and semantics of grammatical discrete structures, Artif. Intell. Eng. Design Anal. Manuf. 13 (4) (1999) 241–251, https://doi.org/10.1017/S0890060499134012.

[70] P. Geyer, Multidisciplinary grammars supporting design optimization of buildings, Res. Eng. Des. 18 (4) (Jan. 2008) 197–216, https://doi.org/10.1007/s00163-007-0038-6.

[71] Y.A.S. Essawy, K. Nassar, Elemental graph data model: a semantic and topological representation of building elements, World Acad. Sci. Eng. Technol. Int. J. Civil Environ. Eng. 11 (6) (Aug. 2017) 845–856, https://doi.org/10.5281/ZENODO.1132216.

[72] E. Durmisevic, Transformable Building Structures. Design for Dissassembly as a Way to Introduce Sustainable Engineering to Building Design & Construction, PhD Thesis, Technische Universiteit Delft, 2006. ISBN: 9789090203416.

[73] K. Kingsland, Comparative analysis of digital photogrammetry software for cultural heritage, Digital Appl. Archaeol. Cultural Heritage 18 (Sep. 2020), e00157, https://doi.org/10.1016/j.daach.2020.e00157.

[74] I. Djuric, I. Vasiljević, M. Obradovic, V. Stojakovic, J. Kicanovic, R. Obradovic, Comparative Analysis of Open-Source and Commercial Photogrammetry Software for Cultural Heritage, in: Proceedings of the 39th International Hybrid Conference on Education and Research in Computer Aided Architectural Design in Europ, Sep. 2021, pp. 49–58, https://doi.org/10.52842/conf.ecaade.2021.2.243.

[75] A. Javaheri, C. Brites, F. Pereira, J. Ascenso, Subjective and objective quality evaluation of 3D point cloud denoising algorithms, in: 2017 IEEE International Conference on Multimedia and Expo Workshops, Jul. 2017, pp. 1–6, https://doi.org/10.1109/ICMEW.2017.8026263.

[76] J. Desai, J. Liu, R. Hainje, R. Oleksy, A. Habib, D. Bullock, Assessing vehicle profiling accuracy of handheld LiDAR compared to terrestrial laser scanning for crash scene reconstruction, Sensors 21 (23) (Jan. 2021), https://doi.org/10.3390/s21238076. Art. no. 23.

[77] A. Spreafico, F. Chiabrando, L. Teppati Losè, F. Giulio Tonolo, The ipad pro built-in lidar sensor: 3d rapid mapping tests and quality assessment, in: The International Archives of the Photogrammetry, Remote Sensing and Spatial Information Sciences XLIII-B1–2021, Jun. 2021, pp. 63–69, https://doi.org/10.5194/isprs-archives-XLIII-B1-2021-63-2021.

[78] J. Canny, A computational approach to edge detection, IEEE Trans. Pattern Anal. Mach. Intell. PAMI-8 (6) (Nov. 1986) 679–698, https://doi.org/10.1109/TPAMI.1986.4767851.

[79] R.O. Duda, P.E. Hart, Use of the Hough transformation to detect lines and curves in pictures, Commun. ACM 15 (1) (Jan. 1972) 11–15, https://doi.org/10.1145/361237.361242.

[80] M. Ester, H.-P. Kriegel, J. Sander, X. Xu, A Density-Based Algorithm for Discovering Clusters in Large Spatial Databases with Noise, in: *Proceedings of the Second International Conference on Knowledge Discovery and Data Mining*, Portland, Oregon, 1996, pp. 226–231. ISBN: 978-1-57735-418-5.

[81] D. Wolleb-Graf, Digraph Reachability Algorithms, Doctoral Thesis, ETH Zurich, 2018, https://doi.org/10.3929/ethz-b-000321834.

[82] H. Fan, H. Su, L. Guibas, A Point Set Generation Network for 3D Object Reconstruction from a Single Image, in: 2017 IEEE Conference on Computer Vision and Pattern Recognition, Dec. 2016, pp. 2463–2471, https://doi.org/10.1109/CVPR.2017.264.

[83] E. Iacovidou, P. Purnell, Mining the physical infrastructure: opportunities, barriers and interventions in promoting structural components reuse, Sci. Total Environ. 557–558 (Jul. 2016) 791–807, https://doi.org/10.1016/j.scitotenv.2016.03.098.

[84] T. Krijnen, J. Beetz, An IFC schema extension and binary serialization format to efficiently integrate point cloud data into building models, Adv. Eng. Inform. 33 (Aug. 2017) 473–490, https://doi.org/10.1016/j.aei.2017.03.008.

[85] M. Gordon, R. Vargas, Mattersite: Circularizing Demolition Waste with Digitization and Machine Learning Strategies, Masters Thesis, Institute for Advanced Architecture of Catalonia, Barcelona, 2021 (Not Available Online).